Design and characterization of a low cost CubeSat multi-band optical receiver to map water ice on the lunar surface for the Lunar Flashlight mission

Quentin Vinckier[a], Karlton Crabtree[b], Christopher G. Paine[a], Paul O. Hayne[a], Glenn R. Sellar[a]
[a]California Institute of Technology, Jet Propulsion Laboratory, 4800 Oak Grove Dr, Pasadena, CA, USA 91109; [b]Photon Engineering LLC, 310 S Williams Blvd #222, Tucson, AZ, USA 85711

ABSTRACT

Lunar Flashlight is an innovative NASA CubeSat mission dedicated to mapping water ice in the permanently shadowed regions of the Moon, which may act as cold traps for volatiles. To this end, a multi-band reflectometer will be sent to orbit the Moon. This instrument consists of an optical receiver aligned with four lasers, each of which emits sequentially at a different wavelength in the near-infrared between 1 µm and 2 µm. The receiver measures the laser light reflected from the lunar surface; continuum/absorption band ratios are then analyzed to quantify water ice in the illuminated spot. Here, we present the current state of the optical receiver design. To optimize the optical signal-to-noise ratio, we have designed the receiver so as to maximize the laser signal collected, while minimizing the stray light reaching the detector from solar-illuminated areas of the lunar surface outside the field-of-view, taking into account the complex lunar topography. Characterization plans are also discussed. This highly mass- and volume-constrained mission will demonstrate several firsts, including being one of the first CubeSats performing science measurements beyond low Earth orbit.

Keywords: NASA Lunar Flashlight mission, NIR optical receiver, NIR multi-band reflectometer, CubeSat

1. INTRODUCTION

For nearly a century, predictions have been made for the existence of stable ice deposits in the Permanently Shadowed Regions (PSRs) of the Moon[1,2]. In such PSRs located near the lunar poles, temperatures are low enough (≤110 K) to trap lunar volatiles, such as H_2O, NH_3, CO_2 or H_2S, in their solid state[3–5]. Mapping and quantifying lunar volatiles, in particular water, associated with these cold traps addresses one of NASA's (National Aeronautics and Space Administration) strategic knowledge gaps to understand the lunar resource potential for future human exploration of the moon[6]. In addition, these data are also crucial to address outstanding questions in planetary science, such as testing hypotheses regarding the delivery and retention of water and other volatiles in the inner solar system.

Over the last two decades, several flyby missions have revealed strong indications of the presence of lunar water ice using a wide range of techniques such as magnitude and/or polarization analysis of radar signal[7–9], hydrogen measurements using neutron spectrometry[10–16], proton albedo measurements[17], UV spectrometry[4,18–21], visible-wavelength spectrometry[20,21], NIR (Near-InfraRed) 1.2-2.4 µm spectrometry[20], NIR 3 µm absorption-based spectrometry[22–24], 1 µm reflectivity measurements[25–27]. However, there remain open questions about the interpretation of some of the measurements. Some data are ambiguous and often lead to conflicting science conclusions[3,5,13,25]. Complementary data based on other detection techniques are thus necessary to improve our knowledge and refute or corroborate the previous results. The LF (Lunar Flashlight) CubeSat mission is designed to identify and map water ice in the permanently shadowed regions of the Moon by measuring surface reflectance at zero-phase angle with four different wavelength bands in the NIR region. LF will be one of the first CubeSats performing science measurements beyond low Earth orbit – two other CubeSat missions have been selected to make complementary lunar volatile measurements[28,29] – and the first planetary mission to use multi-band active reflectometry from orbit. One of these bands, centered in 1064 nm, has been chosen to enable science results comparison with LOLA (Lunar Orbiter Laser Altimeter), which used 1064 nm lasers[25–27]. Although LOLA was firstly designed to map the lunar topography[30,31], this instrument was also capable of measuring reflectance of the Moon at 1064 nm and at zero-phase angle like the LF instrument[30–33].

After a brief description of the mission in the next section, this paper focuses on the receiver optical design, as well as on its characterization bench design.

2. MISSION OVERVIEW

The Lunar Flashlight mission is an innovative NASA 6U (6 Units of approximately 10×10×10 cm each) CubeSat mission dedicated to mapping water ice in the PSRs within 10° latitude of the lunar south pole. The measurement approach utilizes a multi-band reflectometer in orbit at the Moon. The CubeSat will be launched as a secondary payload on the first test flight of the SLS (Space Launch System), currently planned to launch in 2019. The instrument payload consists of an optical receiver aligned with four lasers, which sequentially emit 1 ms pulses with optical output powers of 10-35 W. Ideally, each laser shall emit in a different wavelength band centered in the NIR spectral region: 1.064 µm +/- 20 nm, 1.495 µm +/- 20 nm, 1.85 µm +20/-30 nm and 1.99 µm +25/-20 nm with a maximum FWHM (Full width at Half Maximum) of 20 nm. These wavelengths correspond to peak absorption wavelengths for water ice and nearby continuum wavelengths. The optical receiver collects and measures a portion of the laser light reflected from the lunar surface; reflectance and continuum/absorption reflectance band ratios are then analyzed to quantify water ice in the illuminated spot (see Figure 1). The full mission success criteria are to be able to identify locations where water ice is present at concentrations ≥0.5wt% (0.5 weight %) in the lunar surface and with a mapping resolution of 1 km. During the approximately 2-month primary mission, LF will pulse the lasers for several minutes on each orbit, near its ~14 km perilune over the south polar region.

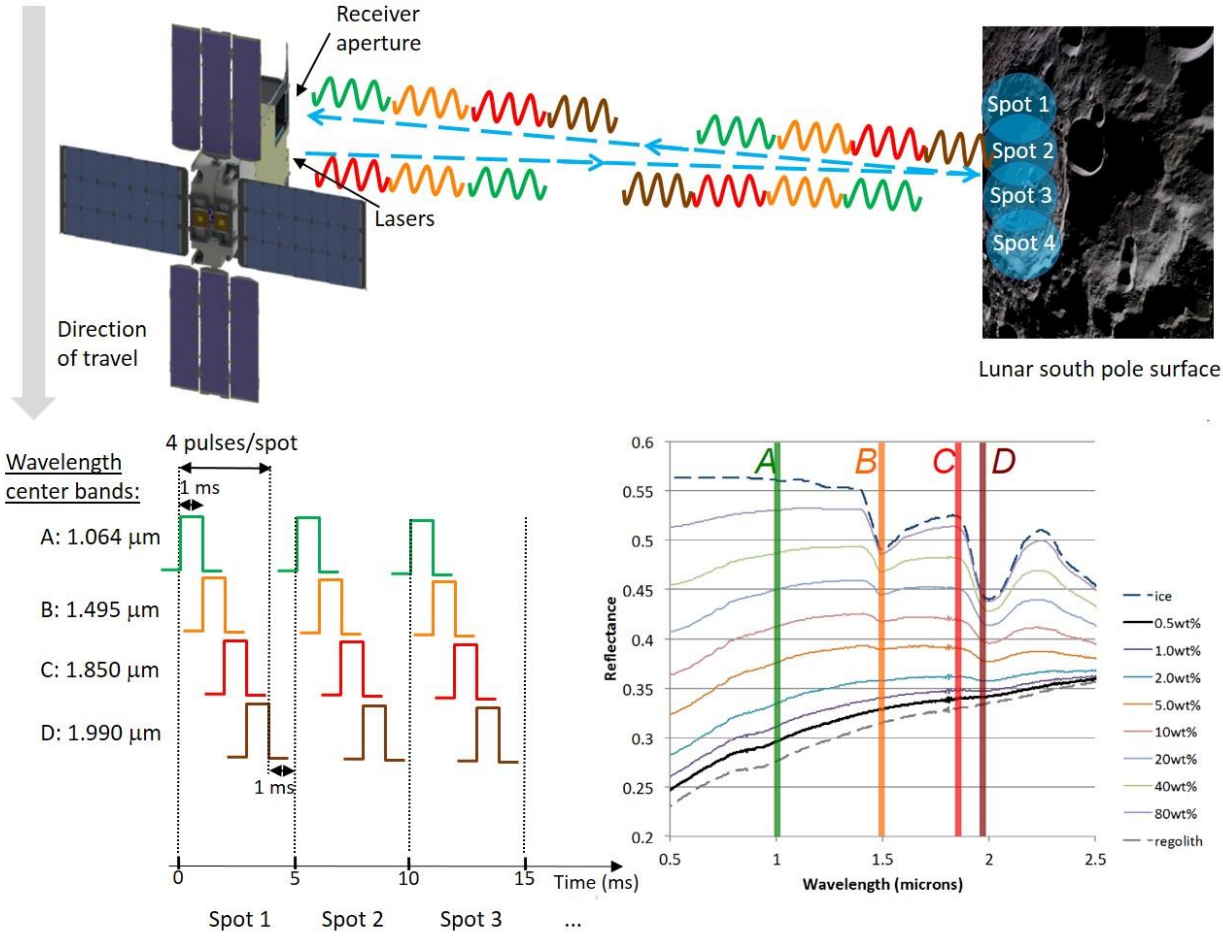

Figure 1. Lunar Flashlight CubeSat mission overview. The lasers fire sequentially for 1 ms, followed by a pause for 1 ms with all lasers off. This latter measurement quantifies the sum of detector dark current, instrument background, detected ambient (solar) illumination from within the FOV (Field-Of-View), and stray light from outside the FOV. In data processing, this background is subtracted from the measured signals for each laser pulse to derive the reflectance of the lunar surface at each of the four wavelengths. Reflectance and absorption/continuum reflectance band ratios are then analyzed to quantify the weight % of water ice at the lunar surface.

3. OPTICAL DESIGN OF THE RECEIVER

3.1 First approximation of the required receiver field-of-view

The detailed optical design of the receiver has been completed by Photon Engineering using the FRED software. The receiver has to be as simple as possible, given the volume, mass and cost constraints of a CubeSat mission. We have based the optical design on a single, off-aperture, aluminum paraboloid mirror with a single-pixel detector located at the focus.

The receiver FOV (Field-Of-View) has to cover the beam divergence profiles of the lasers in order to maximize the light reaching the detector active area, taking into account the lasers co-alignment. Figure 2 shows the normalized simulated beam divergence profiles for each of the four lasers already mounted in the "laser package". These data come from DILAS Inc. (Diode LASer Inc.), which has designed the lasers we will use. The data coordinates refer to an orthonormal 3-axis coordinate system attached to the "laser package" with the z-axis perpendicular to the optical window of the laser package; lasers co-alignment is thus "included" in the data depicted in Figure 2. By calculating the centroid of each divergence profile, we have evaluated a co-alignment full-angle of 0.17°. This angle represents twice the smallest polar angle containing the centroid of each laser beam divergence profile.

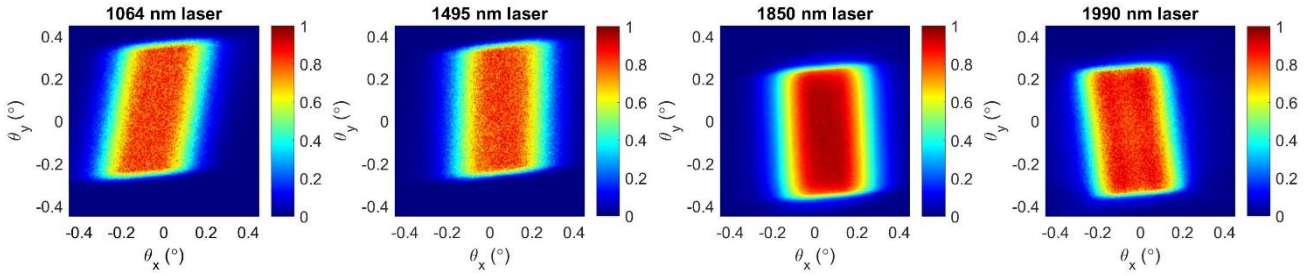

Figure 2. Normalized lasers beam divergence profiles. The color scales report the lasers radiances normalized to unity. θ_x and θ_y are respectively the rotation angles around axis X and Y, XY plane being coplanar with the optical window of the lasers package.

In order to model the signal (number of photons) reaching the detector, we have used what we call a "composite source", which is the average beam divergence profile of the four lasers normalized to one. This normalized average beam divergence profile is depicted in Figure 3, as well as its corresponding normalized encircled energy VS (VerSus) polar angle.

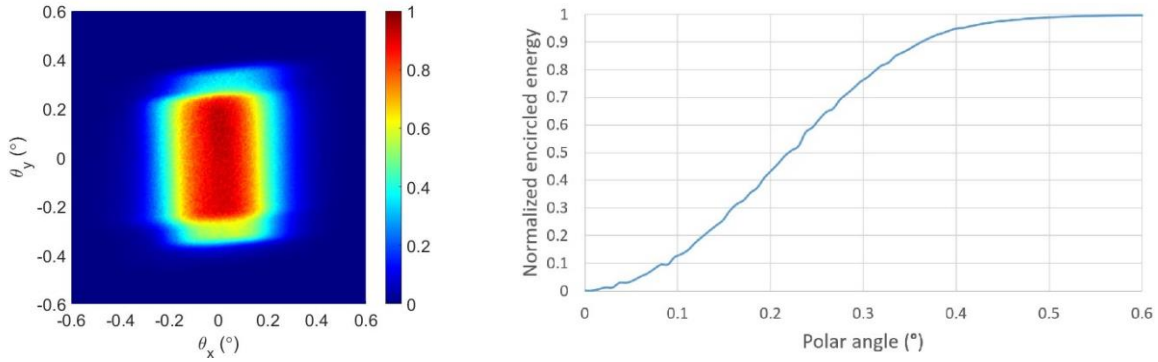

Figure 3. Normalized average beam divergence profile and normalized encircled energy. The color scale reports the average lasers radiance normalized to unity, whereas the encircled energy is normalized by the total energy emitted by the composite source. θ_x and θ_y are respectively the rotation angles around axis X and Y, XY plane being coplanar with the optical window of the lasers package. Using the small angle approximation, the polar angle is equal to $(\theta_x^2+\theta_y^2)^{1/2}$.

Using the composite source emitting toward an off-axis paraboloid mirror, we have modeled the relative number of photons reaching a detector active surface of 0.5 mm and 1 mm diameter for different mirror focal lengths. The detector

defocus around the focal position was optimized in order to maximize the lasers power on the detector active area. This analysis assumes a mirror reflectivity of 100% and a detector surface reflectivity of 0%, which means that the only losses are due to geometric aberrations. The results are reported on Figure 4.

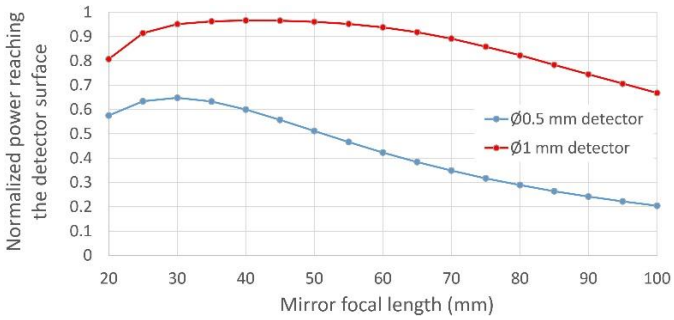

Figure 4. Normalized power reaching the detector active area VS the paraboloid mirror focal length for two different detector active surface diameters. Y-axis reports the power reaching the detector active area normalized by the total power incident on the mirror.

Using the paraxial approximation, the theoretical FOV of an optical system with a detector located at the focal position is given by FOV=2×arctan(Ø/[2×FL]), where Ø is the diameter of the detector and FL is the mirror Focal Length. Figure 4 shows that despite having a greater theoretical FOV/2 than the polar angle corresponding to almost 100% of encircled energy for the composite source, a significant fraction of the flux collected by the mirror misses the 0.5 mm diameter detector for a mirror focal length of 30 mm. Indeed, for Ø=0.5 mm and FL=30 mm, FOV/2=0.48° and 64% of the lasers power reaches the detector active area (see Figure 4), whereas the encircled energy of the composite source is equal to 98.5% for a polar angle of 0.48°. These high optical aberrations are due to the fact that we consider very fast and off-axis paraboloid mirrors in this analysis.

Choosing the optimal detector active surface diameter and mirror focal length based on the results given in Figure 4 is challenging in this particular case. On one hand, the 1 mm diameter detector offers a larger receiver detection efficiency. On the other hand, it also increases the receiver FOV and thus the background coming from the detected solar-illumination of the lunar surface from within the FOV, as well as the background coming from solar-illumination of the lunar surface scattered to the detector active area from outside the FOV (i.e. stray light). During operation, we do acquire background measurements (with all lasers off) for background subtraction, and the corresponding shot noise in background measurements constitutes a source of noise on the measured reflected lasers signal after background subtraction. Background depends on the lunar topography and on the exact trajectory of the CubeSat for a given receiver design[33]. At this early design phase, given that we are primary interested in mapping water ice into the PSRs, we have first assumed that the major background contribution is that reflected from solar-illuminate areas of the lunar surface outside the FOV of the receiver (i.e. stray light). Following this assumption, the 1 mm diameter detector is the optimized choice to maximize the optical signal-to-noise ratio. The maximum detected power is given for FL=40 mm. However, decreasing the FOV by increasing the FL only slightly affects the detection efficiency in a certain FL range, and could potentially be beneficial to decrease the background shot noise, leading thus to increase the optical signal-to-noise ratio. Quite arbitrarily, as a first draft design, we have decided to choose a focal length of 70 mm. This reduces the FOV by a factor of 1.75 and only decreases the detected power by a factor of 7.8%.

3.2 Stray light analysis and current optical design

Once the detector diameter and the mirror focal length have been chosen, we have designed baffles to minimize stray light on the detector active area. The stray light scattering model used by the FRED software is based on the Harvey-Shack surface scatter theory[34]. All internal surfaces are modeled as painted with flat black paint and the mirror scatter was modeled as 30 Å roughness and CL450[35] particulates (0.164% percent area coverage).

In order to predict the science performance of a given receiver optical design, our mission-level performance model uses the receiver PST (Point Source Transmittance) function calculated in FRED[33]. This is basically the fraction of flux at the receiver aperture that reaches the detector active area as a function of the θ_x and θ_y field angles. It thus represents the receiver detection efficiency as a function of θ_x and θ_y. Different configurations have been analyzed with our mission performance model to come out with the optimized receiver optical design depicted in Figure 5. Table 1 lists the principal

technical specifications of the receiver design. Figure 6 shows the predicted rotationally averaged PST function of the current receiver optical design depicted in Figure 5.

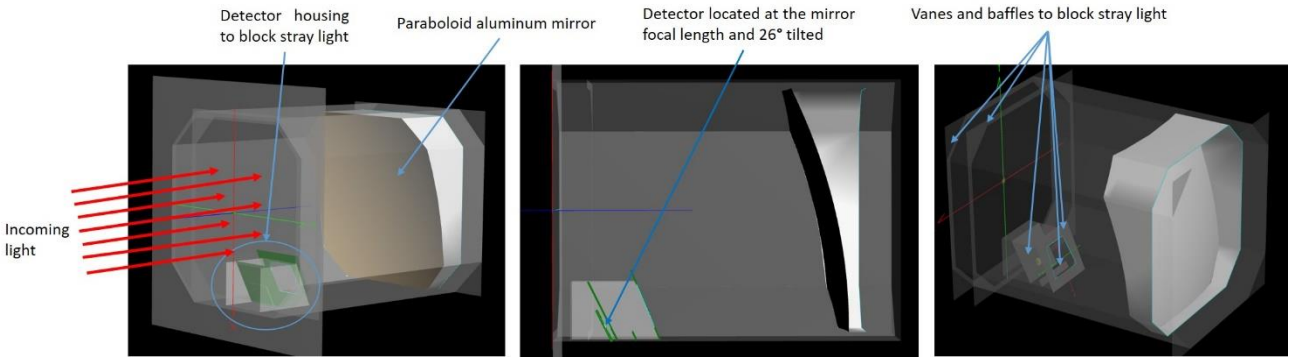

Figure 5. Receiver optical design.

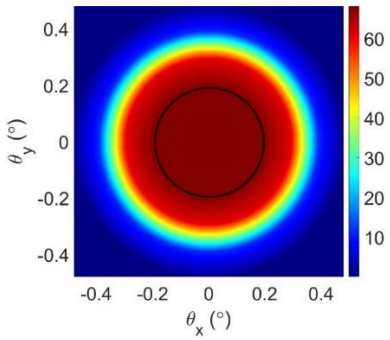

Figure 6. Receiver Point Source Transmittance (PST) function. Using the small angle approximation, values reported are average values for each polar angle $(\theta_x^2+\theta_y^2)^{1/2}$.The color scale represents the percent of flux at the receiver aperture that reaches the detector. The theoretical FOV/2 of the receiver is equal to a polar angle of arctan(Ø/[2×FL])=arctan(1/[2×70)≈0.4°. However, the maximal PST value of the central plateau does not correspond to angles for which $(\theta_x^2+\theta_y^2)^{1/2}$=0.4°, but rather $(\theta_x^2+\theta_y^2)^{1/2}$=0.2° in our case (see the area on the figure within the black circle). This is an effect caused by geometric aberrations. The maximum value of the PST is equal to 68%, which is quite far from 100%. The primary reason for this is the PST calculation is performed with a 75 mm square entrance aperture, rather than the smaller and more complex mirror shape of the actual receiver. Additional power losses come from the mirror reflectivity modeled as 94.5% (reflectance of Al at a wavelength of 1 µm), the detector surface reflectivity modeled as 3%, and losses due to vignetting by the detector housing (which obstructs a part of the receiver aperture).

Table 1. Principal technical specifications of the current receiver design.

Receiver dimensions	100×75×75 mm
Receiver aperture	75×75 mm
Mirror surface	• Bare aluminum off-axis paraboloid mirror, assuming post-polish • Radius of curvature: 140 mm • Surface accuracy: 2λ @ 632.8 nm • RMS (Root Mean Square) roughness: <30 Å
Detector	• 2.2 µm cutoff InGaAs Teledyne Judson 1 mm diameter detector • Thermally isolated from the receiver structure and passively cooled by a cryo-radiator (not presented in this paper)

3.3 Receiver-to-lasers alignment stability

The lasers power back-reflected from the lunar surface and detected by the receiver is given by

$$P_{detected,\lambda} = P_{emitted,\lambda} \times R_\lambda \times \int \mathrm{PST}_\lambda(\theta_x - \delta_x, \theta_y - \delta_y)\mathrm{LDP}_\lambda(\theta_x, \theta_y)\mathrm{d}\theta_x d\theta_y, \quad (1)$$

where δ_x and δ_y are the misalignment angles between the lasers and the receiver, $\mathrm{PST}_\lambda(\theta_x,\theta_y)$ is the receiver PST for a wavelength λ, $\mathrm{LDP}_\lambda(\theta_x,\theta_y)$ is the Laser Divergence Profile normalized by the integrated radiance over θ_x and θ_y for the laser emitting at a wavelength center band λ, $P_{emitted,\lambda}$ is the total power emitted at a wavelength center band λ and R_λ is the fraction of the emitted laser power for a wavelength center band λ that reaches the receiver aperture after being back-reflected from the lunar surface. For the sake of simplicity, this model assumes that the lasers spectral profiles do not depend on the divergence angles θ_x and θ_y. This may not be the case in practice. However, this can be neglected for the conclusions of the analysis developed in this section.

For $\delta_x \neq 0°$ and/or $\delta_y \neq 0°$, if the receiver FOV is not large enough, SE (Systematic Errors) will appear on the detected power because the instrument is calibrated for an alignment corresponding to $\delta_x=\delta_y=0°$. These SE are given by

$$SE(\%) = \frac{\int \mathrm{PST}_\lambda(\theta_x,\theta_y)\mathrm{LDP}_\lambda(\theta_x,\theta_y)\mathrm{d}\theta_x d\theta_y - \int \mathrm{PST}_\lambda(\theta_x-\delta_x,\theta_y-\delta_y)\mathrm{LDP}_\lambda(\theta_x,\theta_y)\mathrm{d}\theta_x d\theta_y}{\int \mathrm{PST}_\lambda(\theta_x,\theta_y)\mathrm{LDP}_\lambda(\theta_x,\theta_y)\mathrm{d}\theta_x d\theta_y} \times 100. \quad (2)$$

These SE cannot be corrected, as it is usually hard to predict/calibrate the exact optics misalignment occurring during operation due to alignment instabilities. However, it is possible to predict the AS (Alignment Stability) for given simulated temperature gradients, opto-mechanical design of the entire instrument (lasers, receiver, and mounting structure), etc. We define the AS as the maximal value of the polar misalignment angle between the lasers and the receiver. Knowing the AS, we define the relative uncertainty Δ (%) of the detected optical power due to receiver-to-lasers misalignments as

$$\Delta = max\left[\left|\frac{\int \mathrm{PST}_\lambda(\theta_x,\theta_y)\mathrm{LDP}_\lambda(\theta_x,\theta_y)\mathrm{d}\theta_x d\theta_y - \int \mathrm{PST}_\lambda(\theta_x-\delta_x,\theta_y-\delta_y)\mathrm{LDP}_\lambda(\theta_x,\theta_y)\mathrm{d}\theta_x d\theta_y}{\int \mathrm{PST}_\lambda(\theta_x,\theta_y)\mathrm{LDP}_\lambda(\theta_x,\theta_y)\mathrm{d}\theta_x d\theta_y} \times 100\right|\right]_{\forall \sqrt{\delta_x^2+\delta_y^2} \leq AS}. \quad (3)$$

Figure 7 shows the SE of our current receiver optical design as a function of δ_x and δ_y for each laser, considering the lasers beam divergence profiles – which take into account the lasers co-alignment – depicted in Figure 2.

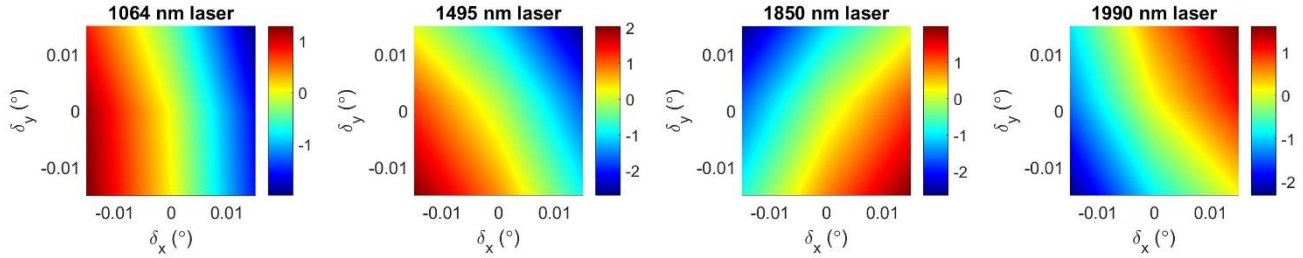

Figure 7. Systematic error (%) on the detected optical power as a function of the receiver-to-lasers misalignment angles. This analysis assumes that the instrument is calibrated for $\delta_x=\delta_y=0°$, where δ_x and δ_y represent the receiver-to-lasers misalignment angles due to alignment instabilities during operation.

We are currently working on the instrument opto-mechanical design to know what AS and Δ we can achieve. Increasing the receiver FOV leads to decrease Δ. However, let us remember that the larger the FOV is, the larger the background illumination shot noise will be on the detected signal. Therefore, the FOV has to be optimized to decrease the overall signal uncertainty. As an example, Figure 8 shows the evolution of the worst-case Δ VS central plateau polar angle for a receiver-to-lasers alignment stability of 0.01°, considering the lasers beam divergence profiles depicted in Figure 2.

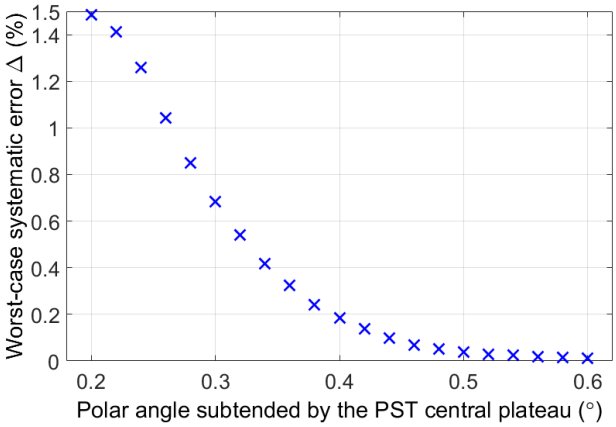

Figure 8. Relative uncertainty on the detected optical power caused by receiver-to-lasers alignment instabilities as a function of the polar angle corresponding to the PST central plateau for a hypothetical AS=0.01°.

The next step is to evaluate the alignment stability we can achieve and optimize the FOV to decrease the overall signal uncertainty. To this end, we will estimate the worst-case Δ for different hypothetical PSTs by increasing the polar angle corresponding to the central plateau of the current PST ($(\theta_x^2+\theta_y^2)^{1/2}$=0.2° is the polar angle corresponding to the central plateau of the current design; see Figure 6). Using these hypothetical PSTs and their corresponding worst-case Δ into our mission-level performance model, we will identify the hypothetical PST that optimizes the overall science results. Then, we will update the current receiver optical design to achieve this optimal PST, model the PST corresponding to the updated optical design with FRED, evaluate the corresponding worst-case Δ, and simulate the corresponding science results with our mission performance model to make sure that they meet our expectations.

4. DESIGN OF THE RECEIVER CHARACTERIZATION BENCH

The receiver spectral response has to be characterized before launch over the intended spectral ranges, taking into account the range of possible band centers and FWHM bandwidths mentioned in section 2: 1.064 µm, 1.495 µm, 1.85 µm, 1.99 µm ±50 nm. This will be done by measuring the output current of the detector as a function of the optical power at the receiver aperture, the wavelength, the detector temperature, and the receiver mirror temperature.

The signal generated by detector dark current and instrument background (photons thermally emitted by the receiver structure and incident on the detector active area) will be characterized as a function of the detector temperature and the receiver structure temperature. This will be achieved by simply turning off the receiver aperture illumination, given that the detector will be isolated from other external photon sources than the structure of the receiver itself.

The receiver PST will also be characterized using a two-axis goniometer on which the receiver will rest. A uniform collimated beam will illuminate the receiver aperture with a known and stable optical power, and we will measure the output detector current as a function of θ_x and θ_y scanned by the goniometer. This will be done as a function of the detector temperature and the receiver structure temperature because they can both affect the geometry of the receiver and thus its PST.

The goal is to characterize the receiver in similar conditions occurring during operation:

- The optical input power for which we expect to extract usable measurements is in the range [0.5, 50] nW;
- The temperature range of the detector during operation is [-165,-41] °C (a margin of -15 °C is included on the lowest temperature and a margin of +20 °C is taken on the highest temperature);
- The temperature range of the receiver structure during operation is [-65,7] °C (a margin of -15 °C is included on the lowest temperature and a margin of +20 °C is taken on the highest temperature);
- The receiver will be tested in a vacuum chamber. A vacuum of 10^{-5} Torr has been chosen as a reasonable value for testing.

The cost constraints of a CubeSat mission also limit the test equipment available, so the test bench design is as simple as possible and utilizes COTS (Commercial Off-The-Shelf) components to the extent possible while achieving a reasonable characterization uncertainty. The design of the characterization bench is presented in Figure 9. As a first test, we will characterize the detector linearity (we expect the detector to be linear up to 1 mW optical power). Before testing the receiver, we will calibrate this bench for each key parameter: optical power at the receiver aperture, wavelength, temperature control of the detector and temperature control of the receiver structure. The characterization bench will be controlled via LabView to make the characterization measurements autonomous.

The illumination source depends on the test. We will use a monochromater coupled with a customized fiber bundle to characterize the receiver spectral response with a ≤4 nm spectral resolution. This monochromater is provided by the vendor with its light source already pre-aligned. The fiber bundle will collect the light at the monochromater exit slit and send a part of it (minimum 20 nW after the optical window in the worst case) to the receiver aperture through a fiber-coupled reflective collimator, and the other part (minimum 50 nW after the optical window in the worst case) to an OPM (Optical Power Monitoring) chain consisting of a low noise pyroelectric sensor used with an optical chopper and a lock-in amplifier. The noise on each optical power measurement will be as low as ~5 nW RMS. Before each measurement, a diaphragm will cut off the illumination of the pyroelectric sensor to take a dark frame and adjust the measure in consequence. The OPM chain will be calibrated to know the illumination power at the receiver aperture. In order to not have to characterize the OPM chain as a function of the wavelength, we will simulate the vacuum chamber window by inserting an identical window in the OPM chain. In addition, to send light on the active area of the pyroelectric sensor, we will also use the same reflective collimator (silver coated reflective collimator) as the one used to illuminate the receiver aperture, but with a different size. The choice of a low-noise pyroelectric sensor compared to a semiconductor sensor has also been made so as not to have to characterize the OPM chain as a function of the wavelength. Indeed, our pyroelectric sensor has a very low and linear spectral dependence in the 1-2 µm NIR region that has already been characterized by the detector vendor with a high accuracy. This test bench design constitutes a low cost and almost "plug-and-play" solution (no time-consuming alignment needed) to spectrally characterize our receiver, and each measurement can be repeated many times to decrease its uncertainty. As an example, by repeating 400 times each measurement, we will be able to measure the relative optical power sent towards the receiver in the 1-2 µm NIR spectral range with a worst-case uncertainty of $\sigma_{OPM,n=400}$=[5 nW/(50 nW×$\sqrt{400}$)]×100=0.5% (we can neglect the nonlinearity of the OPM chain in the optical power range we measure). As the current of the receiver detector will be measured with an accuracy of $\Delta_{det.\ current}$≤0.25%, we expect to be able to characterize the relative spectral response of the receiver with a worst-case error of ± ($\sigma_{OPM,n=400}$+$\Delta_{det.\ current}$), so ± 0.75%. Given that the RMS noise corresponding to the measured current of the receiver detector will not exceed 0.01%, only the nonlinearity of the pico-ammeter would have to be taken into account in the accuracy calculation related to the relative receiver detector current measurement. However, because we do not have this technical specification, we consider here the calibration accuracy $\Delta_{det.\ current}$ of our pico-ammeter (which includes the equipment nonlinearity and the accuracy of the calibration source, as well as some margins).

The illumination source used to characterize the receiver PST will be a fiber-coupled laser module emitting at 660 nm. This module will allow us to characterize the PST with a very stable and higher optical power (tens of µW with only ≤0.1% power instability during 15 minutes of operation) compared to the one available at the monochromater output, leading to quick measurements at high accuracy. Of course, we will previously make sure that the detector remains in its linear regime using this power magnitude order. The reflective collimator used to characterize the receiver PST has been designed to reach a full-angle beam divergence of ≤0.01°, corresponding to the available angle resolution for the PST characterization. Another advantage of this fiber-coupled laser module is that the output light can be modulated at up to 100 kHz with a simple analog input voltage. This will be used to simulate real illumination conditions by pulsing light toward the receiver when the instrument will be tested with its flight electronics.

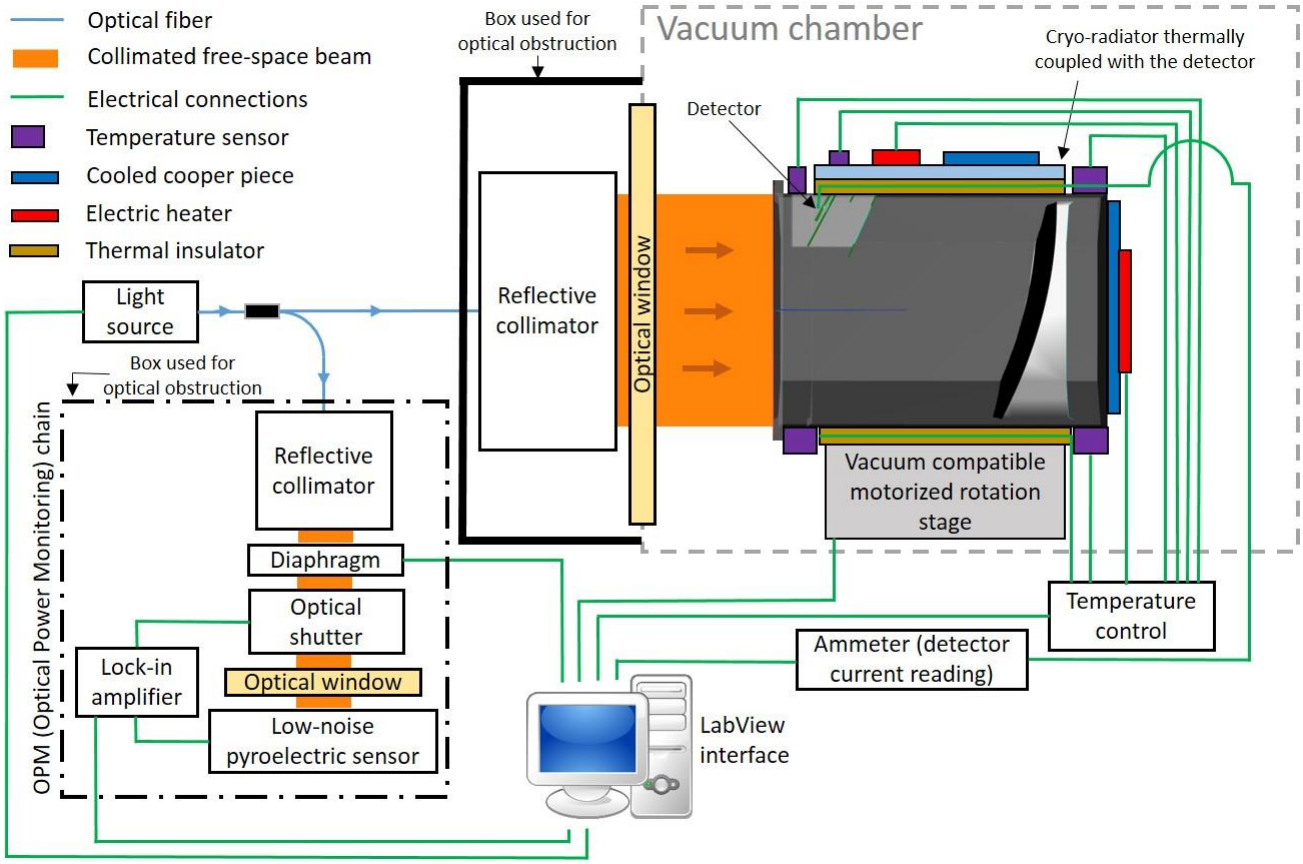

Figure 9. Receiver characterization bench. The temperature of the detector and the receiver structure will be stabilized independently using a cryogenic cooling system, several electric heaters and several temperature sensors interfaced to a PID (Proportional–Integral–Derivative) regulator running on the computer. The number of heaters, temperature sensors and their locations still have to be chosen.

5. CONCLUSIONS

Lunar Flashlight is an innovative NASA CubeSat mission dedicated to mapping water ice in the permanently shadowed regions of the lunar south pole by measuring surface reflectance at multiple wavelengths. The instrument payload consists of an optical receiver – based on an off-axis paraboloid mirror focusing incoming light onto a single detector – aligned with four near-infrared lasers, which are fired sequentially.

Two main topics are discussed in this paper. The first one is focused on the optical receiver design. We can point out two main steps in the receiver optical design in our particular case. First, the mirror focal length and the detector active surface diameter have to be chosen to maximize the detected lasers signal reflected from the lunar surface. Then, the second step consists in optimizing the optical design to minimize stray light, which is solar-illumination of the lunar surface reflected toward the receiver outside its FOV and scattered in the “receiver box” toward the detector active area. Stray light and light coming from the solar-illumination of the lunar surface reflected within the receiver FOV contribute to background to the received flux. During operation, we do acquire background measurements (with all lasers off) for background subtraction, and the corresponding shot noise in background measurements constitutes a source of noise on the measured reflected lasers signal after background subtraction. The science performance of our instrument is highly sensitive to this solar-illumination related noise, which depends on the lunar topography and thus on the exact orbits of the CubeSat. Increasing the detector active area and optimizing the mirror focal length to maximize the detected lasers light will also increase the solar-illumination related noise. Given that we are primary interested in mapping water ice into the PSRs, we have first assumed that the major contribution of noise is given by solar-illumination of the lunar surface back-reflected toward the instrument outside (and not inside) its FOV (i.e. stray light). Following this assumption, a 1 mm diameter

detector active surface has been identified as the optimal choice to maximize the optical signal-to-noise ratio. Despite that the maximum detected power is given for a mirror focal length of 40 mm for this detector active area, we have decided to base our first draft design on a mirror focal length of 70 mm. This only slightly affects the detection efficiency, whereas it decreases the background shot noise. This current receiver configuration optimized to minimize stray light reaching the detector has shown good science performance using our mission performance model. We are currently working on the instrument opto-mechanical design to determine what receiver-to-lasers alignment stability we can achieve. Increasing the receiver FOV leads to decrease the corresponding uncertainty Δ on the detected power which is due to receiver-to-lasers alignment instabilities, but it also increases the background shot noise. Therefore, the FOV has to be optimized in order to decrease the overall signal uncertainty. To this end, we still have the flexibility to adjust the receiver FOV by changing the mirror focal length and/or the detector size if necessary.

The second topic discussed in this paper is the characterization bench design of the receiver. Four technical features have to be characterized: the detector linearity VS the power at the receiver aperture, the receiver spectral response VS the detector temperature and the receiver mirror temperature, the receiver point source transmittance function VS the detector temperature and the receiver structure temperature, and the detector signal due to the detector dark current and due to the photons thermally emitted by the receiver structure and seen by the detector VS the detector temperature and the receiver structure temperature. We have designed a simple (almost "plug-and-play") low-cost characterization bench based on commercial off-the-shelf components. All the key parameters – i.e. optical power at the receiver aperture, wavelength, temperature of the detector and temperature of the receiver structure – will be controlled via LabView to make the characterization measurements autonomous.

This highly mass- and volume-constrained instrument payload will demonstrate several firsts, including being one the first instruments onboard a CubeSat performing science measurements beyond low Earth orbit and the first planetary mission to use multi-band active reflectometry from orbit.

ACKNOWLEDGMENT

The Lunar Flashlight mission is funded by the Advanced Exploration Systems program in the Human Exploration and Operations (HEO) mission directorate of the National Aeronautics and Space Administration (NASA). We acknowledge DILAS Inc. for the design of the lasers. Part of this work was performed at the Jet Propulsion Laboratory, California Institute of Technology, under contract with NASA.

REFERENCES

[1] Goddard, R. H., [The Papers of Robert H. Goddard: 1898-1924], McGraw-Hill, New York, 413-430 (1970).

[2] Watson, K., Murray, B. and Brown, H., "On the possible presence of ice on the Moon," Journal of Geophysical Research 66(5), 1598-1600 (1961).

[3] Paige, D. A., Siegler, M. A., Zhang, J. A., Hayne, P. O., Foote, E. J., Bennett, K. A., Vasavada, A. R., Greenhagen, B. T., Schofield, J. T., McCleese, D. J., Foote, M. J., DeJong, E., Bills, B. G., Hartford, W., Murray, B. C., Allen, C. C., Snook, K., Soderblom, L. A., Calcutt, S., Taylor, F. W., Bowles, N. E., Bandfield, J. L., Elphic, R., Ghent, R., Glotch, T. D., Wyatt, M. B. and Lucey P. G., "Diviner lunar radiometer observations of cold traps in the Moon's south polar region," Science 330(6003), 479-482 (2010).

[4] Hayne, P. O., Hendrix, A., Sefton-Nash, E., Siegler, M. A., Lucey, P. G., Retherford, K. D., Williams, J. P., Greenhagen, B. T. and Paige, D. A., "Evidence for exposed water ice in the Moon's south polar regions from Lunar Reconnaissance Orbiter ultraviolet albedo and temperature measurements," Icarus 255, 58-69 (2015).

[5] Hayne, P. O., Paige, D. A., Ingersoll, A. P., Judd, M. A., Aharonson, O., Alkali, L., Byrne, S., Cohen, B., Colaprete, A., Combe, J. P. and Edwards, C., "New Approaches to Lunar Ice Detection and Mapping: Study Overview and Results of the First Workshop," Report of the Annual Meeting of the Lunar Exploration Analysis Group 1748, 7043 (2013).

[6] The Lunar Exploration Analysis Group (LEAG), the Mars Exploration Program Analysis Group (MEPAG) and the Small Bodies Assessment Group (SBAG), "Strategic Knowledge Gaps (SKGs)," NASA, 29 August 2016, < https://www.nasa.gov/exploration/library/skg.html > (19 September 2016).

[7] Thomson, B. J., Bussey, D. B. J., Neish, C. D., Cahill, J. T. S., Heggy, E., Kirk, R. L., Patterson, G. W., Raney, R. K., Spudis, P. D., Thompson, T. W. and Ustinov, E. A., "An upper limit for ice in Shackleton crater as revealed by LRO Mini-RF orbital radar," Geophysical Research Letters 39(14) (2012).
[8] Spudis, P. D., Bussey, D. B. J., Baloga, S. M., Cahill, J. T. S., Glaze, L. S., Patterson, G. W., Raney, R. K., Thompson, T. W., Thomson, B. J. and Ustinov, E. A., "Evidence for water ice on the Moon: Results for anomalous polar craters from the LRO Mini-RF imaging radar," Journal of Geophysical Research: Planets 118(10), 2016-2029 (2013).
[9] Nozette, S., Lichtenberg, C. L., Spudis, P., Bonner, R., Ort, W., Malaret, E., Robinson, M. and Shoemaker, E. M., "The Clementine bistatic radar experiment," Science 274(5292), 1495-1498 (2016).
[10] Feldman, W. C., Maurice, S., Binder, A. B., Barraclough, B. L., Elphic, R. C. and Lawrence, D. J., "Fluxes of fast and epithermal neutrons from Lunar Prospector: Evidence for water ice at the lunar poles," Science 281(5382), 1496-1500 (1998).
[11] Feldman, W. C., Lawrence, D. J., Elphic, R. C., Barraclough, B. L., Maurice, S., Genetay, I. and Binder, A. B., "Polar hydrogen deposits on the Moon," Journal of Geophysical Research 105(E2), 4175-4195 (2000).
[12] Feldman, W. C., Lawrence, D. J., Little, R. C., Lawson, S. L., Gasnault, O., Wiens, R. C., Barraclough, B. L., Elphic, R. C., Prettyman, T. H. and Steinberg, J. T., "Evidence for water ice near the lunar poles," Journal of Geophysical Research, 106(E10), 23231-23251 (2001).
[13] Mitrofanov, I. G., Sanin, A. B., Boynton, W. V., Chin, G., Garvin, J. B., Golovin, D., Evans, L. G., Harshman, K., Kozyrev, A. S., Litvak, M. L. and Malakhov, A., "Hydrogen mapping of the lunar south pole using the LRO neutron detector experiment LEND," Science 330(6003), 483-486 (2010).
[14] Mitrofanov, I., Litvak, M., Sanin, A., Malakhov, A., Golovin, D., Boynton, W., Droege, G., Chin, G., Evans, L., Harshman, K. and Fedosov, F., "Testing polar spots of water-rich permafrost on the Moon: LEND observations onboard LRO," Journal of Geophysical Research: Planets 117(E12) (2012).
[15] Boynton, W. V., Droege, G. F., Mitrofanov, I. G., McClanahan, T. P., Sanin, A. B., Litvak, M. L., Schaffner, M., Chin, G., Evans, L. G., Garvin, J. B. and Harshman, K., "High spatial resolution studies of epithermal neutron emission from the lunar poles: Constraints on hydrogen mobility," Journal of Geophysical Research: Planets 117(E12) (2012).
[16] Livengood, T. A., Chin, G., Sagdeev, R. Z., Mitrofanov, I. G., Boynton, W. V., Evans, L. G., Litvak, M. L., McClanahan, T. P., Sanin, A. B. and Starr, R. D., "Evidence for Diurnally Varying Hydration at the Moon's Equator from the Lunar Exploration Neutron Detector (LEND)," Proc. Lunar and Planetary Science Conference 45, 1507 (2014).
[17] Schwadron, N. A., Wilson, J. K., Looper, M. D., Jordan, A. P., Spence, H. E., Blake, J. B., Case, A. W., Iwata, Y., Kasper, J. C., Farrell, W. M. and Lawrence, D. J., "Signatures of volatiles in the lunar proton albedo," Icarus 273, 25-35 (2016).
[18] Gladstone, G. R., Retherford, K. D., Egan, A. F., Kaufmann, D. E., Miles, P. F., Parker, J. W., Horvath, D., Rojas, P. M., Versteeg, M. H., Davis, M. W. and Greathouse, T. K., "Far-ultraviolet reflectance properties of the Moon's permanently shadowed regions," Journal of Geophysical Research: Planets 117(E12) (2012).
[19] Hendrix, A. R., Retherford, K. D., Randall Gladstone, G., Hurley, D. M., Feldman, P. D., Egan, A. F., Kaufmann, D. E., Miles, P. F., Parker, J. W., Horvath, D. and Rojas, P. M., "The lunar far-UV albedo: Indicator of hydration and weathering," Journal of Geophysical Research: Planets 117(E12) (2012).
[20] Colaprete, A., Schultz, P., Heldmann, J., Wooden, D., Shirley, M., Ennico, K., Hermalyn, B., Marshall, W., Ricco, A., Elphic, R. C. and Goldstein, D., "Detection of water in the LCROSS ejecta plume," Science 330(6003), 463-468 (2012).
[21] Heldmann, J. L., Lamb, J., Asturias, D., Colaprete, A., Goldstein, D. B., Trafton, L. M. and Varghese, P. L., "Evolution of the dust and water ice plume components as observed by the LCROSS visible camera and UV–visible spectrometer," Icarus 254, 262-275 (2015).
[22] Pieters, C. M., Goswami, J. N., Clark, R. N., Annadurai, M., Boardman, J., Buratti, B., Combe, J. P., Dyar, M. D., Green, R., Head, J. W. and Hibbitts, C., "Character and spatial distribution of OH/H2O on the surface of the Moon seen by M3 on Chandrayaan-1," Science 326(5952), 568-572 (2009).
[23] Sunshine, J. M., Farnham, T. L., Feaga, L. M., Groussin, O., Merlin, F., Milliken, R. E. and A'Hearn, M. F., "Temporal and spatial variability of lunar hydration as observed by the Deep Impact spacecraft," Science 326(5952), 565-568 (2009).
[24] Clark, R. N., "Detection of adsorbed water and hydroxyl on the Moon," Science 326(5952), 562-564 (2009).
[25] Zuber, M. T., Head, J. W., Smith, D. E., Neumann, G. A., Mazarico, E., Torrence, M. H., Aharonson, O., Tye, A. R., Fassett, C. I., Rosenburg, M. A. and Melosh, H. J., "Constraints on the volatile distribution within Shackleton crater at the lunar south pole," Nature 486(7403), 378-381 (2012).

[26] Lucey, P. G., Neumann, G. A., Paige, D. A., Riner, M. A., Mazarico, E. M., Smith, D. E., Zuber, M. T., Siegler, M., Hayne, P. O., Bussey, D. B. J., Cahill, J. T. S., McGovern, A., Isaacson, P., Corley, L. M., Torrence, M. H., Melosh, H. J., Head, J. W. and Song, E., "Evidence for Water Ice and Temperature Dependent Space Weathering at the Lunar Poles from Lola and diviners," Proc. Lunar and Planetary Science Conference 45, 2325 (2014).
[27] Fisher, E. A., Lucey, P. G., Lemelin, M., Greenhagen, B. T., Siegler, M. A., Mazarico, E., Aharonson, O., Williams, J. P., Hayne, P. O., Neumann, G. A. and Paige, D. A., "Evidence for surface water ice in the lunar polar regions using reflectance measurements from the Lunar Orbiter Laser Altimeter and temperature measurements from the Diviner Lunar Radiometer Experiment," Icarus 292, 74-85 (2017).
[28] Clark, P. E., Malphrus, B., Brown, K., Hurford, T., Brambora, C., MacDowall, R., Folta, D., Tsay, M., Brandon, C. and Team, L. I. C., "Lunar Ice Cube: Searching for Lunar Volatiles with a lunar cubesat orbiter," Proc. AAS/Division for Planetary Sciences Meeting 48, 223.03 (2016).
[29] Hardgrove, C., Bell, J., Thangavelautham, J., Klesh, A., Starr, R., Colaprete, T., Robinson, M., Drake, D., Johnson, E., Christian, J. and Genova, A., "The Lunar Polar Hydrogen Mapper (LunaH-Map) mission: Mapping hydrogen distributions in permanently shadowed regions of the Moon's south pole," Proc. Annual Meeting of the Lunar Exploration Analysis Group 1863, 2035 (2015).
[30] Smith, D. E., Zuber, M. T., Neumann, G. A., Lemoine, F. G., Mazarico, E., Torrence, M. H., McGarry, J. F., Rowlands, D. D., Head, J. W., Duxbury, T. H. and Aharonson, O., "Initial observations from the lunar orbiter laser altimeter (LOLA)," Geophysical Research Letters 37(18) (2010).
[31] Riris, H., Cavanaugh, J., Sun, X., Liiva, P., Rodriguez, M. and Neuman, G., "The lunar orbiter laser altimeter (LOLA) on NASA's lunar reconnaissance orbiter (LRO) mission," Proc. International Conference on Space Optics 8 (2010).
[32] Ramos-Izquierdo, L., Scott III, V. S., Connelly, J., Schmidt, S., Mamakos, W., Guzek, J., Peters, C., Liiva, P., Rodriguez, M., Cavanaugh, J. and Riris, H., "Optical system design and integration of the Lunar Orbiter Laser Altimeter," Applied Optics 48(16), 3035-3049 (2009).
[33] Cohen, B. A., Hayne, P. O., Greenhagen, B. T., Paige, D. A., Camacho, J. M., Crabtree, K., Paine, C. G. and Sellar, R. G., "Payload Design for the Lunar Flashlight Mission," Proc. Lunar and Planetary Science Conference 48, 1709 (2017).
[34] Harvey, J., "Light Scattering Characteristics of Optical Surfaces," Ph.D. dissertation, University of Arizona (1976).
[35] MIL-STD-1246C, MILITARY STANDARD: PRODUCT CLEANLINESS LEVELS CONTAMINATION CONTROL PROGRAM, 1994.